Frontiers of Information Technology & Electronic Engineering
www.jzus.zju.edu.cn; engineering.cae.cn; www.springerlink.com
ISSN 2095-9184 (print); ISSN 2095-9230 (online)
E-mail: jzus@zju.edu.cn

Influence of motor cable on common-mode currents in an inverter-fed motor drive system*

Peng-kang XIE[1,2], Jia-zheng LU[2], Guo-zhu CHEN[1], Heng-lin CHEN[†‡1]

[1]*College of Electrical Engineering, Zhejiang University, Hangzhou 310027, China*

[2]*State Key Laboratory of Disaster Prevention & Reduction for Power Grid Transmission and Distribution Equipment, State Grid Hunan Electric Power Corporation Disaster Prevention & Reduction Center, Changsha 410007, China*

[†]E-mail: henglin@zju.edu.cn

Received Sept. 3, 2016; Revision accepted Dec. 13, 2016; Crosschecked Feb. 15, 2018

Abstract: Induction motor drive systems fed by cables are widely used in industrial applications. However, high-frequency switching of power devices will cause common-mode (CM) voltages during operation, leading to serious CM currents in the motor drive systems. CM currents through the cables and motors in the drive systems can cause electromagnetic interference (EMI) with the surrounding electronic equipment and shorten the life of induction motors. Therefore, it is necessary to analyze the CM currents in motor drive systems. In this paper, high-frequency models of unshielded and shielded power cables are formulated. The frequency-dependent effects and mutual inductances of the cables are taken into account. The power cable parameters are extracted by the finite element method and validated by measurements. High-frequency models of induction motors and inverters are introduced from existing works. The CM currents at the motor and inverter terminals are obtained, and the influence of the cable length and cable type on the CM currents is analyzed. There is a good agreement between the experimental results and the CM currents predicted by the proposed models.

Key words: Common-mode currents; Cable model; Motor drive system; Parameter extraction
https://doi.org/10.1631/FITEE.1601518 **CLC number:** TM12

1 Introduction

Cable-fed adjustable-speed drives (ASDs) are widely used in modern industrial applications (Liu et al., 2013; Hafez et al., 2014; Tseng et al., 2015). The switching operations of the semiconductor devices in pulse width modulation (PWM) inverters can cause common-mode (CM) voltages and CM currents in ASDs (Jiang et al., 2013). A typical ASD is shown in Fig. 1. The ASD is grounded through a ground wire. The conductors of phases *A*, *B*, and *C* in the drive system are contained in a three-wire cable. A grounded conductor *N* is added in a four-wire cable. The grounded conductor and metallic shield for the shielded cable are connected to the ground wires. As shown in Fig. 1, i_a, i_b, and i_c are the phase currents, i_g is the ground current, and i_N is the current flowing in the conductor *N* and the metallic shield. Note that $i_a+i_b+i_c$ means the CM currents measured in this study (Saini et al., 2012; Hoseini et al., 2014). Since the CM currents can shorten the life of induction motors and cause electromagnetic interference (EMI) problems (Erdman et al., 1996; Kerkman et al., 1997), it is important to study the CM currents in ASDs.

Since the transient CM current oscillations range from several kHz to a few MHz, to study the CM currents in ASDs, it is necessary to build high-frequency (several kHz to several MHz) models of the PWM inverter, power cable, and induction motor. Motor models for high-frequency analysis have been proposed and validated in the time and frequency domains (Amarir and Al-Haddad, 2008;

‡ Corresponding author
* Project supported by the National Natural Science Foundation of China (No. 51577172)
ORCID: Heng-lin CHEN, http://orcid.org/0000-0003-3513-0625

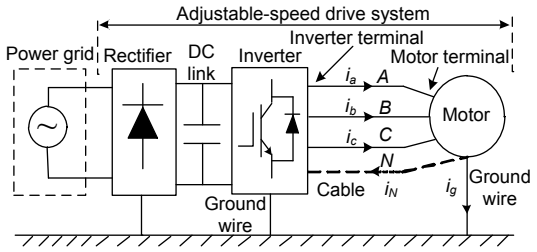

Fig. 1 Schematics of a typical adjustable-speed drive system

Moreau et al., 2009; Wang et al., 2010; Vidmar and Miljavec, 2015). Inverter models have also been presented (Moreau et al., 2009). These models of induction motors and PWM inverters have proved to be effective. Cable models for high-frequency analysis in ASDs were formulated (Weens et al., 2006; de Paula et al., 2008; Magdun et al., 2009), and the circuit elements in the branch models of power cables did not vary with frequency, but they were properly connected resulting in equivalent impedance that could represent the variations in cable parameters with frequencies. The mutual inductances between the conductors in the shielded cables have been modeled (Moreira et al., 2002). However, in the existing works, the mutual inductances between conductors in unshielded cables have not been considered.

Based on the simulation techniques above, the EMIs conducted in ASDs were modeled (Moreau et al., 2009), and the motor terminal over-voltages and ground wire currents were presented, but the influence of the cable parameters was not analyzed. The influence of cables on the motor terminal over-voltages was also studied (Amarir and Al-Haddad, 2008; de Paula et al., 2008; Wang et al., 2010), and the variation of over-voltage amplitudes and oscillation frequencies with different cable lengths were presented, but the influence of cables on the CM currents was not mentioned. The cable parameters' influence on the CM impedance of ASDs was studied (Luszcz, 2011, 2013; Lu et al., 2016), but the cable model was too simple to represent the frequency variation in the cable impedance, and the time-domain waveforms of the CM currents were not presented. According to the current studies, most of them focused on shielded power cables. However, because of the cheap cost, unshielded power cables are frequently used in ASDs despite the EMI (Weens et al., 2006; Magdun et al., 2009; Wang et al., 2010). With regard to unshielded cables, little has been done to study the influence of cable type and cable length on the CM currents in both the time and frequency domains.

In this study, unshielded and shielded cable models are built, accounting for the skin, proximity effects, and dielectric losses of the cables. Contrary to existing works, the mutual inductances between the conductors in unshielded cables are considered. The cable parameters are extracted using the finite element method. Simplified models for the induction motor and inverter are introduced from existing literature (Moreau et al., 2009; Magdun and Binder, 2014), and they are simple in their parameter extraction and accurate for high-frequency analysis. The CM currents of different cable types and cable lengths in ASDs are presented in simulations and validated by experiments. The influence of cable parameters on CM currents is also studied in both the time and frequency domains.

2 High-frequency modeling of cables

2.1 Modeling of power cables

The power cables studied are shown in Fig. 2, and the conductors of phases *A*, *B*, and *C* are contained in the unshielded three-wire cable, while a grounded conductor *N* and a metallic shield are added in the four-wire shielded cable. The conductors are coated with polyvinyl chloride (PVC). The radius of each conductor is 2 mm and the radius of the cable is 8 mm. The metallic shield and conductor *N* are connected to the ground wire of the ASD. The ground wire is modeled by a resistor connected in series with an inductor in this study.

The power cable models presented in this study are based on the transmission line theory. The basic elementary cell of the proposed cable models is shown in Fig. 3. The parasitic capacitance between the unshielded cable and the ground is so small that it is neglected (Luszcz, 2011). For accurate simulations, the length of the elementary cell should be much smaller than the wavelength of the fast transients in the cable, $\lambda=v\cdot\tau_{\mathrm{rise}}$. Here, v is the wave propagation velocity, about 1.5×10^8 m/s, and τ_{rise} is the voltage rise time of the switching devices, chosen as 50 ns

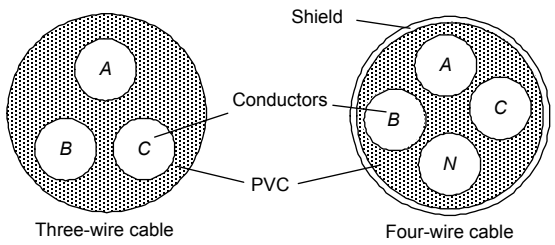

Fig. 2 Cross-sections of the cables

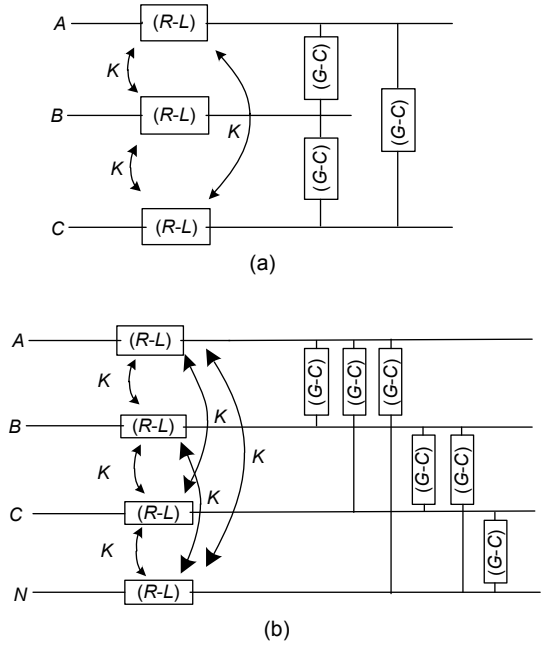

Fig. 3 Basic cell of the cable models: (a) three-wire cable; (b) four-wire cable

(Purcarea et al., 2009). Accordingly, the length of the elementary cell is set to be 1 m.

Because of the skin, proximity effects, and dielectric losses, the cable parameters change over time. The cable models considering the frequency-dependent effects of the cable parameters are shown in Fig. 3, and described as follows (de Paula et al., 2008; Magdun et al., 2009): (1) The *R*-*L* ladder network represents the cable impedance, accounting for the skin and the proximity effects, as well as stray inductances and mutual inductances, and *K* is the mutual inductance coefficient; (2) The *G*-*C* ladder network represents the capacitance and conductance.

The *R*-*L* ladder branch used in this study is shown in Fig. 4a. R_1–R_n represent the resistance of each branch, respectively. L_1–L_n represent the self-inductance of each branch in the *R*-*L* model, respectively. The controlled voltage sources U_1–U_n represent the mutual inductance voltages of each branch, respectively.

The *G*-*C* ladder branch is shown in Fig. 4b. C_1–C_n represent the capacitance of each branch, and G_1–G_n represent the conductance of each branch, respectively.

The *R*-*L* and *G*-*C* elements are different for different conductors, and do not vary with frequency, but are properly connected resulting in equivalence, which represents the frequency-dependence of the impedance and conductance.

A higher branch number in Fig. 4 does not necessarily provide better solutions due to the more complex calculations involved in obtaining the results. Moreover, when an excessive number of branches are used, some of the branch parameters calculated can have negative values, which have no physical meanings (de Paula et al., 2008). In this study, we choose four to be the branch number to provide a satisfactory compromise between simulation duration and model accuracy. When the branch number increases, negative values appear.

The *R*-*L* ladder impedance $Z(f)$ and *G*-*C* ladder admittance $Y(f)$ at frequency f can be written as follows:

$$Z(f)=R(f)+\mathrm{j}\cdot 2\pi fL(f)=\mathrm{j}\cdot 2\pi fL_4+\cfrac{1}{\cfrac{1}{R_4}+\cfrac{1}{\mathrm{j}\cdot 2\pi fL_3+\cfrac{1}{\cfrac{1}{R_3}+\cfrac{1}{\mathrm{j}\cdot 2\pi fL_2+\cfrac{1}{\cfrac{1}{R_2}+\cfrac{1}{\cfrac{1}{R_1}+\mathrm{j}\cdot 2\pi fL_1}}}}}}, \tag{1}$$

$$Y(f)=G(f)+\mathrm{j}\cdot 2\pi fC(f)=\mathrm{j}\cdot 2\pi fC_4+\cfrac{1}{\cfrac{1}{G_4}+\cfrac{1}{\mathrm{j}\cdot 2\pi fC_3+\cfrac{1}{\cfrac{1}{G_3}+\cfrac{1}{\mathrm{j}\cdot 2\pi fC_2+\cfrac{1}{\cfrac{1}{G_2}+\cfrac{1}{\cfrac{1}{G_1}+\mathrm{j}\cdot 2\pi fC_1}}}}}}. \tag{2}$$

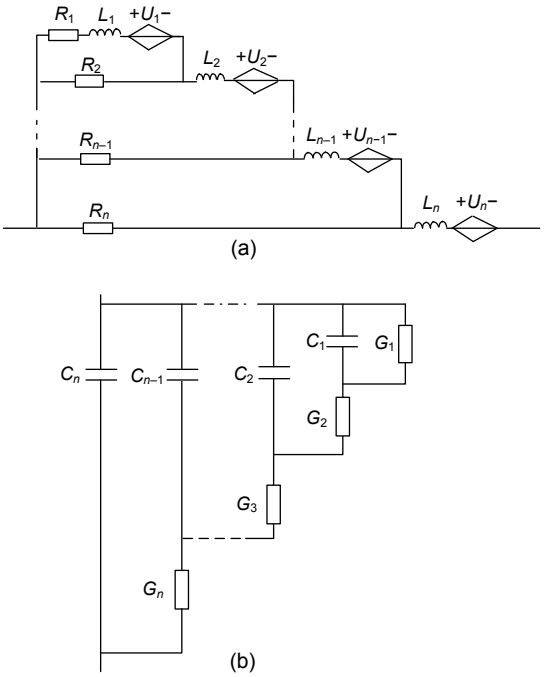

Fig. 4 Ladder circuits in the cable model: (a) *R-L* ladder circuit; (b) *G-C* ladder circuit (Magdun et al., 2009)

In previous studies, the mutual inductance coefficients of the conductors in the unshielded cable were not considered when using an *R-L* ladder network. In this study, controlled voltage sources are proposed to model the mutual inductances between the cable conductors, as shown in Fig. 4a. A mutual inductance coefficient is introduced which remains constant for different branches and different frequencies. The induced voltage of branch m in conductor i produced by the current in conductor j can be written as

$$U_{ij\_m}=K_{ij}L_{im}\left(L_{j1}\frac{\mathrm{d}i_{j1}}{\mathrm{d}t}+L_{j2}\frac{\mathrm{d}i_{j2}}{\mathrm{d}t}+L_{j3}\frac{\mathrm{d}i_{j3}}{\mathrm{d}t}+L_{j4}\frac{\mathrm{d}i_{j4}}{\mathrm{d}t}\right), \tag{3}$$

where L_{im} is the inductance of branch m in conductor i, L_{j1}–L_{j4} are the inductances of each branch in conductor j, i_{j1}–i_{j4} are the currents flowing through each branch of conductor j, and K_{ij} is the mutual inductance coefficient between conductor i and conductor j, which remains constant with frequency f.

2.2 Parameter extraction

An accurate extraction of cable parameters is needed for the calculation of CM currents in motor drive systems. Because of its accuracy and convenience in parameter extraction (Weens et al., 2006), the finite element calculation method is applied to extract the cable parameters using the software named Ansoft. In this study, the cable parameters are calculated in 2D finite element analysis. The copper conductors have a relative permeability of 1, the copper resistivity is 0.0172 μΩ·m, the PVC relative permittivity is 3.5, and the PVC relative permeability is 1.

The finite element meshes of the cables used in this study are shown in Fig. 5. The current densities near the conductor borders are higher at higher frequencies (Cristina and Feliziani, 1989), and to improve the solution accuracy, the meshes near the conductor borders are discretized into smaller elements.

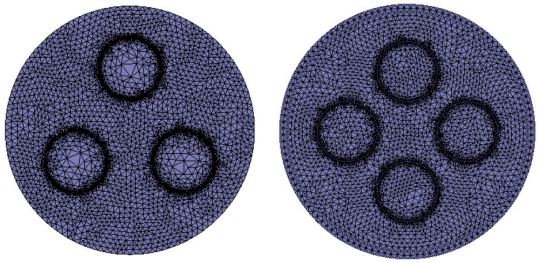

Fig. 5 Cross-sections of finite element meshes: (a) three-wire cable; (b) four-wire cable

The conductor resistances $R(f)$ and inductances $L(f)$ at different frequencies can be obtained from magnetic field analysis. For CM current analysis, a sinusoidal current with an amplitude of 15 mA and a phase of 0° is applied to each phase conductor. In the four-wire cable, a sinusoidal current with an amplitude of 45 mA and a phase of 180° is applied to conductor N. Fig. 6 shows the magnetic field maps when the phase currents reach the maximum value with a 100-kHz current frequency. The resistance of conductor i can be obtained by the power loss of the conductor, $R(f)=P/I^2$, where P is the power loss and I is the conductor current. The self-inductance and mutual inductance can be obtained by

$$L_i(f)=\frac{\psi_i}{I_i}, \tag{4}$$

$$M_{ij}(f)=\frac{\psi_{ij}}{I_i}, \tag{5}$$

$$K_{ij}=\frac{\psi_{ij}}{\psi_i}, \tag{6}$$

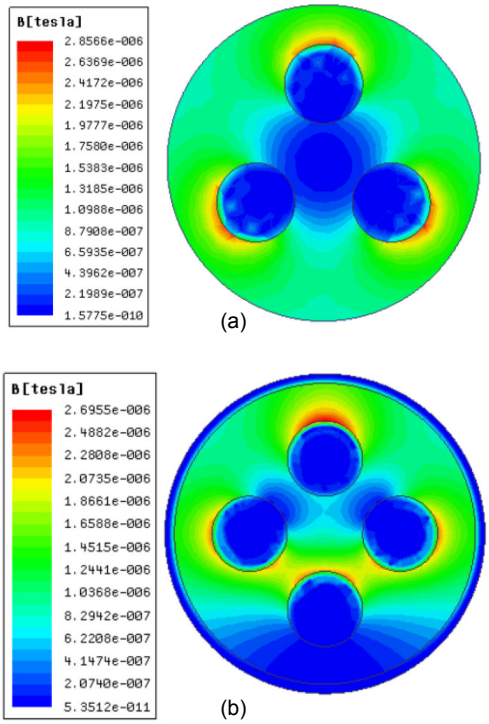

Fig. 6 Magnetic field maps: (a) three-wire cable; (b) four-wire cable (References to color refer to the online version of this figure)

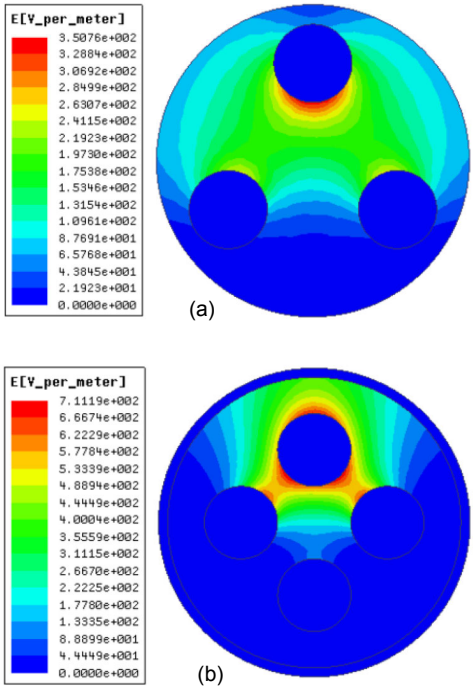

Fig. 7 Electric field maps: (a) three-wire cable; (b) four-wire cable (References to color refer to the online version of this figure)

where $L_i(f)$ is the self-inductance of conductor i, $M_{ij}(f)$ is the multi-inductance between conductor i and conductor j, I_i is the current in conductor i, ψ_i is the flux linkage of conductor i, ψ_{ij} is the flux linkage of conductor j produced by the current in conductor i, and K_{ij} is the mutual inductance coefficient between conductor i and conductor j.

The capacitance $C(f)$ and conductance $G(f)$ between the conductors at different frequencies can be obtained from electric field analysis. Taking conductor A as an example, a sinusoidal voltage with an amplitude of 1 V is applied to conductor A while a 0-V voltage is applied to the other conductors. Fig. 7 shows the electric field maps when the phase A voltage reaches the maximum value with a 100-kHz voltage frequency. Evaluating the electric charge induced in the other conductors, the capacitances between conductor A and the other conductors can be calculated from the relation between the electric charge and the corresponding potential difference. Using this method, the mutual capacitance C between each two conductors can also be obtained. The conductance G between each two conductors can be obtained if the loss tangent $\tan\delta$ is known, $G(f)=2\pi fC\cdot\tan\delta$. The loss tangent at various frequencies for different materials can be chosen from data sheets (Magdun et al., 2009).

Using the finite element method, the cable parameters at different frequencies can be obtained. According to the calculation method proposed by de Paula et al. (2008), the values of ladder circuit elements can be obtained from these cable parameters. In this study, four frequencies (1 kHz, 10 kHz, 100 kHz, and 1 MHz) are chosen, MATLAB software is used to calculate the ladder circuit elements, and the parameter values are given in Tables 1–4.

2.3 Experimental validation

The cable model is validated experimentally. As shown in Fig. 8, an impedance analyzer (HP4294A) is used to measure cable impedance, and the measured cables are 1-m long and placed in straight. The test setup for the three-wire cable is shown in Fig. 8a, where the conductors of phases A and B are connected in parallel, and then connected in series with phase C in a short-circuit test. In the open-circuit test, phases A

and *B* are connected in parallel and disconnected from phase *C*. In the short-circuit test of the four-wire cable (Fig. 8b), phases *A*, *B*, and *C* are connected in parallel, and then the three conductors are connected in series with a metallic shield and conductor *N*. In the open-circuit test of the four-wire cable, the three phases are connected in parallel and disconnected from the shield and conductor *N*.

Fig. 9a shows the impedance frequency response of the three-wire cable per unit length, and Fig. 9b is the impedance frequency response of the four-wire cable per unit length. In Fig. 9, Z_{short} means the

Table 1 *R-L* ladder circuit parameter values per unit length

Branch number	Three-wire (*A*, *B*, *C*)		Four-wire (*A*, *B*, *C*)		Four-wire (*N*)	
	R (mΩ)	*L* (nH)	*R* (mΩ)	*L* (nH)	*R* (mΩ)	*L* (nH)
1	635	479	635	479	445.3	339.3
2	80.6	58.7	80.6	58.7	55.3	42.8
3	22.5	48.6	22.5	48.6	15.31	17.3
4	237.1	235	237.1	235	181.8	176.7

Table 2 Mutual inductance coefficients

Branch	Three-wire	Four-wire
A-B	0.71	0.82
A-C	0.71	0.82
B-C	0.71	0.79
A-N	–	0.85
B-N	–	0.87
C-N	–	0.87

Table 3 *G-C* ladder circuit parameters of the three-wire cable per unit length

Branch number	*A-B* (*B-C*, *A-C*)	
	C (pF)	*G* (μS)
1	635	479
2	80.6	58.7
3	22.5	48.6
4	237.1	235

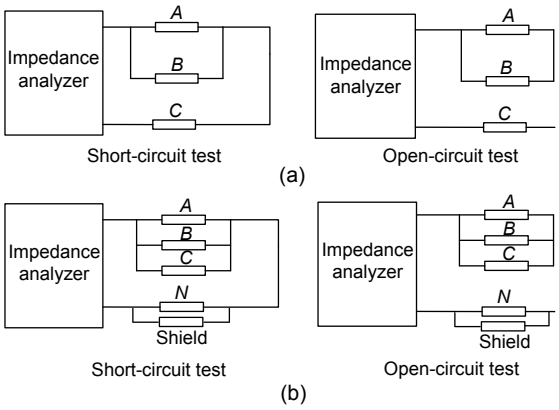

Fig. 8 Impedance frequency response test of the cable: (a) three-wire cable; (b) four-wire cable

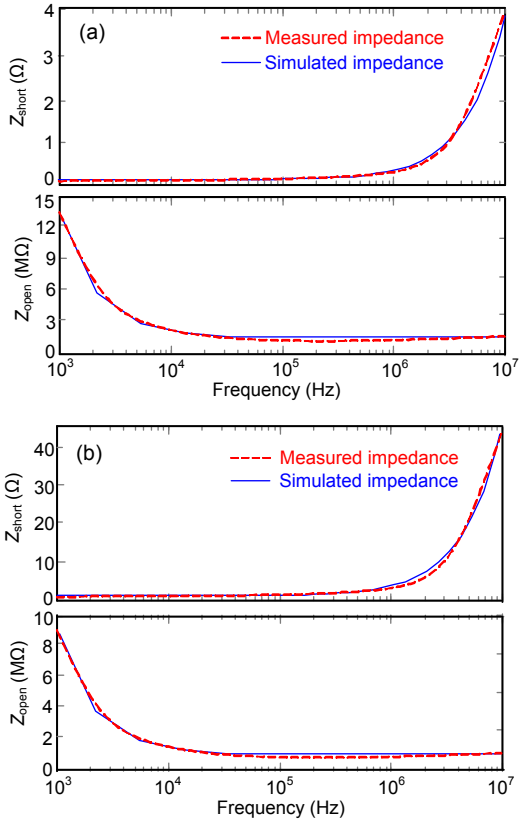

Fig. 9 Impedance frequency response of the cable in per unit length: (a) three-wire cable; (b) four-wire cable

Table 4 *G-C* ladder circuit parameters for the four-wire cable per unit length

Branch number	*A-B* (*A-C*)		*B-C*		*B-N* (*C-N*)		*A-N*	
	C (pF)	*G* (μS)	*C* (pF)	*G* (μS)	*C* (pF)	*G* (μS)	*C* (pF)	*G* (μS)
1	0.004	0.006	0.0029	0.004	0.011	0.021	0.009	0.013
2	3.79	0.04	2.71	0.025	11.41	0.11	7.61	0.09
3	7.98	1.31	5.61	0.95	24.07	4.01	15.94	2.65
4	46.1	7.62	23.25	5.21	138.3	23.13	93.5	15.36

short-circuit impedance and Z_{open} means the open-circuit impedance measured in Fig. 8. Comparing the simulated and measured results, the calculation method has sufficient accuracy to extract the cable parameters from 1 kHz to 10 MHz.

3 Modeling of the induction motor and inverter

3.1 Modeling of the induction motor

Modeling of the induction motor is another key factor for CM current analysis. A per-phase high-frequency motor model shown in Fig. 10 is introduced to analyze the CM currents (Magdun and Binder, 2014). The overall high-frequency three-phase equivalent motor circuit model can be obtained by the connection of three single-phase circuits.

According to Magdun and Binder (2014), the parameters in Fig. 10 can be obtained by measurements and analytical calculation methods. The parameter values of the motor model are shown in Table 5.

3.2 Modeling of the PWM inverter

The high-frequency model of the PWM inverter is shown in Fig. 11 (Moreau et al., 2009). A sinusoidal pulse width modulation (SPWM) algorithm, with a 5-kHz carrier frequency, is used to control the inverter switching devices. Using the method proposed by Moreau et al. (2009), the parasitic circuit parameters are obtained and given in Table 6.

4 Simulation and measurement

The CM currents at the motor and inverter terminals are obtained by simulations according to the models presented. To validate the simulation models, experimental tests are performed. As shown in Fig. 12, the ASD used is composed of a 10-kW inverter (HLP-A100), a straight cable, and an induction motor (power rating 3 kW). Current probes, with a bandwidth from 200 Hz to 10 MHz, are placed at the output terminal of the inverter and the input terminal of the motor. The output signals from the current probes are connected to an oscilloscope (bandwidth from 1 Hz to 100 MHz) to measure the waveform of the CM current i_{CM} ($i_{\text{CM}}=i_a+i_b+i_c$). The sampling rate of the oscilloscope is 1 GHz. It is confirmed that the CM currents have nothing to do with the working condition of the motor, so the CM currents are measured when the induction motor is in a no-load operation.

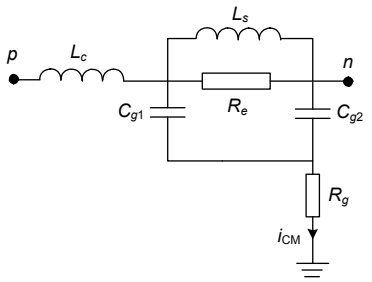

Fig. 10 Per-phase high-frequency motor model (Magdun and Binder, 2014)

C_{g1}: parasitic capacitance between the stator winding and the motor frame; C_{g2}: parasitic capacitance between the stator neutral and the motor frame; R_g: frame ground resistance; L_c: parasitic inductance at the beginning of the winding; L_s: leakage inductance of the winding; R_e: high-frequency resistance of the winding; i_{CM}: CM current that flows through the frame ground resistance R_g

Table 5 Parameter values of the motor model

Parameter	Value	Parameter	Value
L_s (mH)	9.3	C_{g2} (nF)	1.4
L_c (μH)	1.2	R_e (Ω)	5600
C_{g1} (nF)	0.9	R_g (Ω)	15

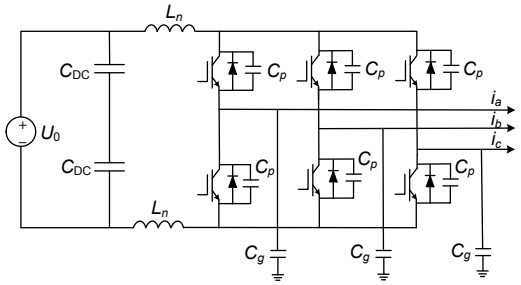

Fig. 11 PWM inverter model (Moreau et al., 2009)

U_0: DC source; C_{DC}: DC capacitance; L_n: stray inductance of the inverter; C_p: capacitance of the inverter; C_g: capacitance between the collector and the heat sink of the switching devices

Table 6 Parameter values of the inverter model

Parameter	L_n (nH)	C_g (nF)	C_p (pF)	C_{DC} (μF)
Value	10	50	100	2200

4.1 Time-domain results

The simulated and measured waveforms from the CM currents for the three-wire 15-m long unshielded cable are shown in Figs. 13a and 13b, and the amplitude variations with different cable lengths are shown in Figs. 13c and 13d. From the comparison between simulated and measured results, it is confirmed that the simulation models considering the mutual inductances can better reflect the experimental results.

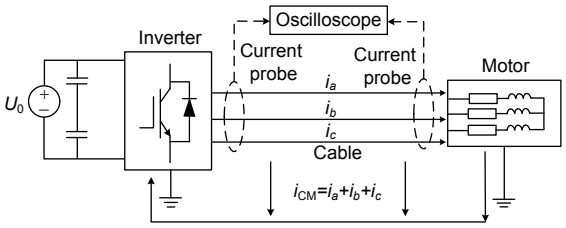

(a)

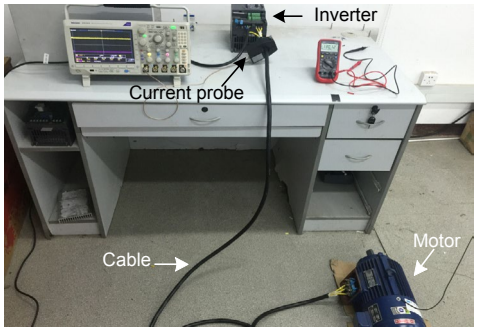

(b)

Fig. 12 Experimental system for CM current measurements: (a) experimental circuit; (b) experimental equipment

From Figs. 13a and 13b, it is observed that the CM currents are damping sinusoidal waveforms caused by the step changes in the CM voltages. From the amplitude variations at different cable lengths shown in Figs. 13c and 13d, it is confirmed that, in the three-wire unshielded cable system, the CM current amplitudes at the inverter terminal are consistent with those at the motor terminal. The CM current amplitude is about 1.5 A when the cable is 15 m long, and the CM current amplitude deceases with the increase of the cable length. The CM current at the motor terminal decreases to a small value (several hundred mA) when the cable is longer than 50 m.

The simulated and measured waveforms for the CM currents with the four-wire 15-m long shielded cable at the inverter and motor terminals are shown in Figs. 14a and 14b. The CM current amplitude variations at different cable lengths are shown in Figs. 14c and 14d. It is confirmed that the simulation models can reflect experimental results with both unshielded and shielded cables.

In Figs. 14a and 14b, when the four-wire shielded cable is 15 m long, the amplitudes of the CM current are about 5 A at the inverter terminal, while they are about 1.5 A at the motor terminal. It is found that, in the four-wire cable system, a large part of the CM current flows through the stray capacitances on the grounded conductor *N* and the metallic shield, and not passing the induction motor. According to Figs. 14c and 14d, the CM current amplitudes increase at the inverter terminal and decrease at the motor terminal with the increase of the cable length.

4.2 Frequency-domain results

The CM currents at the inverter and motor terminals are obtained in the frequency domain. The frequency spectra of the CM currents with different three-wire cable lengths are shown in Figs. 15a and 15b. In the three-wire cable system, when the cable is longer, the dominant CM current frequencies are lower and the amplitudes are smaller. The frequency spectra of the CM currents with different four-wire cable lengths are shown in Figs. 15c and 15d. At the inverter terminal, the dominant CM current frequencies decrease while the amplitudes increase when the cable is longer. However, at the motor terminal, when the cable is longer, the CM current amplitudes decrease.

4.3 Analysis and discussion

According to the simulated and measured results shown above, it is confirmed that the high-frequency model can be used to predict the CM currents with an acceptable accuracy. The equivalent CM circuits of three- and four-wire ASDs are shown in Fig. 16.

As shown in Fig. 16a, in the three-wire cable, the stray capacitances are so small that they can be neglected, and the CM currents' waveforms at the motor terminal are highly consistent with those at the inverter terminal. When the cable length increases, the cable impedance is larger, leading to smaller CM currents at both the inverter and motor terminals.

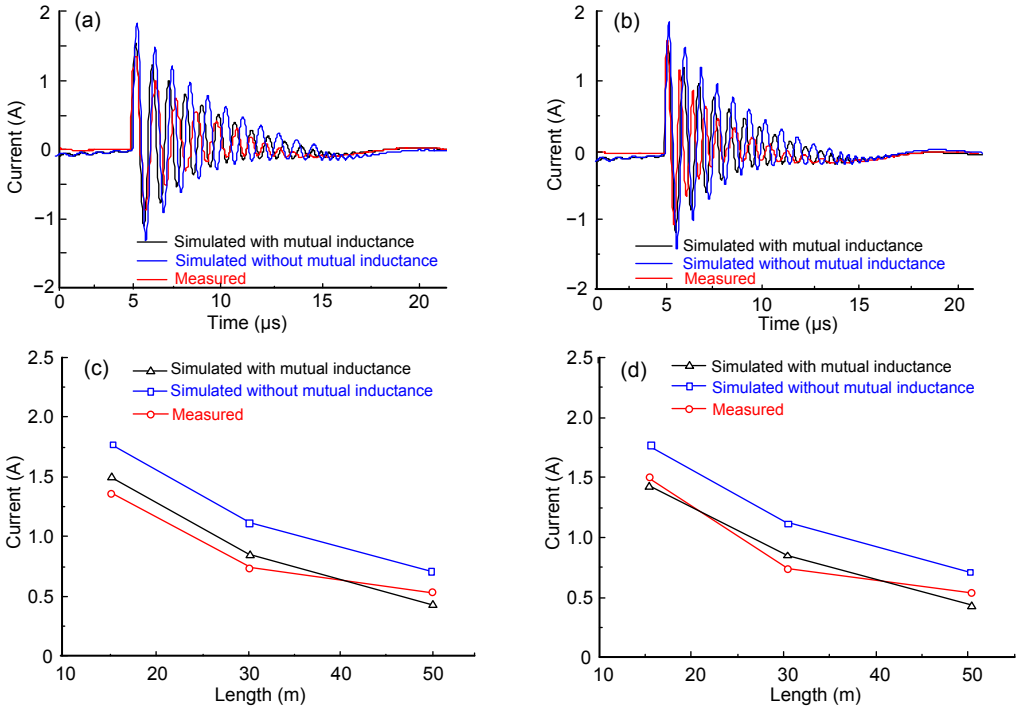

Fig. 13 CM currents with three-wire unshielded cable: (a) waveform with 15-m long cable at inverter terminal; (b) waveform with 15-m long cable at motor terminal; (c) amplitude variations with cable length at inverter terminal; (d) amplitude variations with cable length at motor terminal (References to color refer to the online version of this figure)

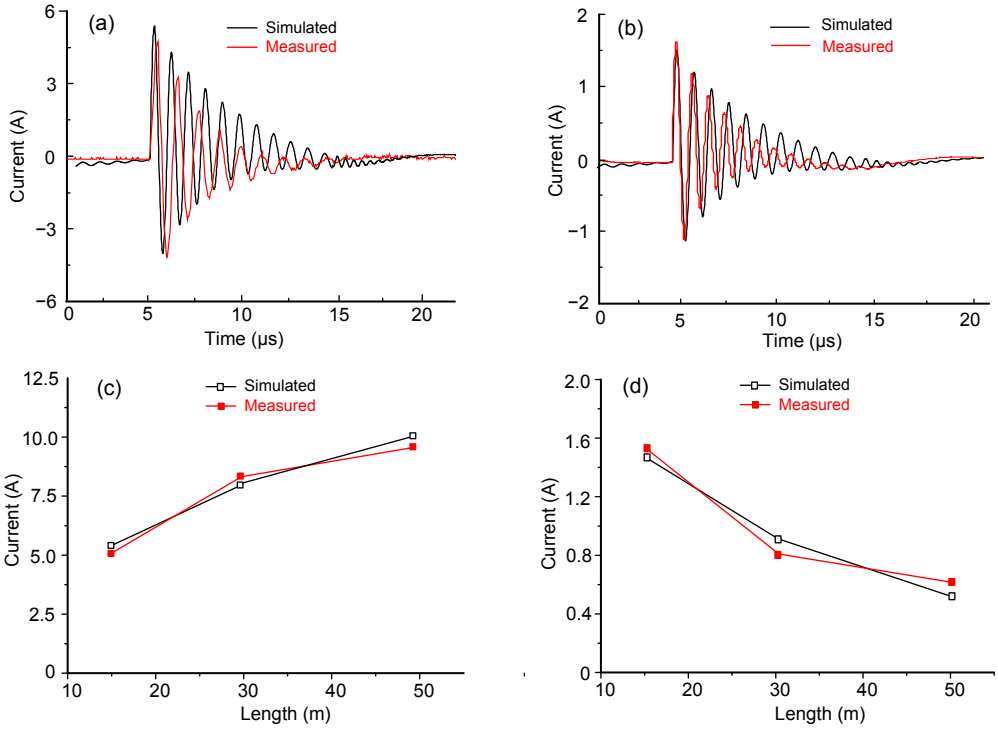

Fig. 14 CM currents with four-wire shielded cable: (a) waveform with 15-m long cable at inverter terminal; (b) waveform with 15-m long cable at motor terminal; (c) amplitude variations with cable length at inverter terminal; (d) amplitude variations with cable length at motor terminal (References to color refer to the online version of this figure)

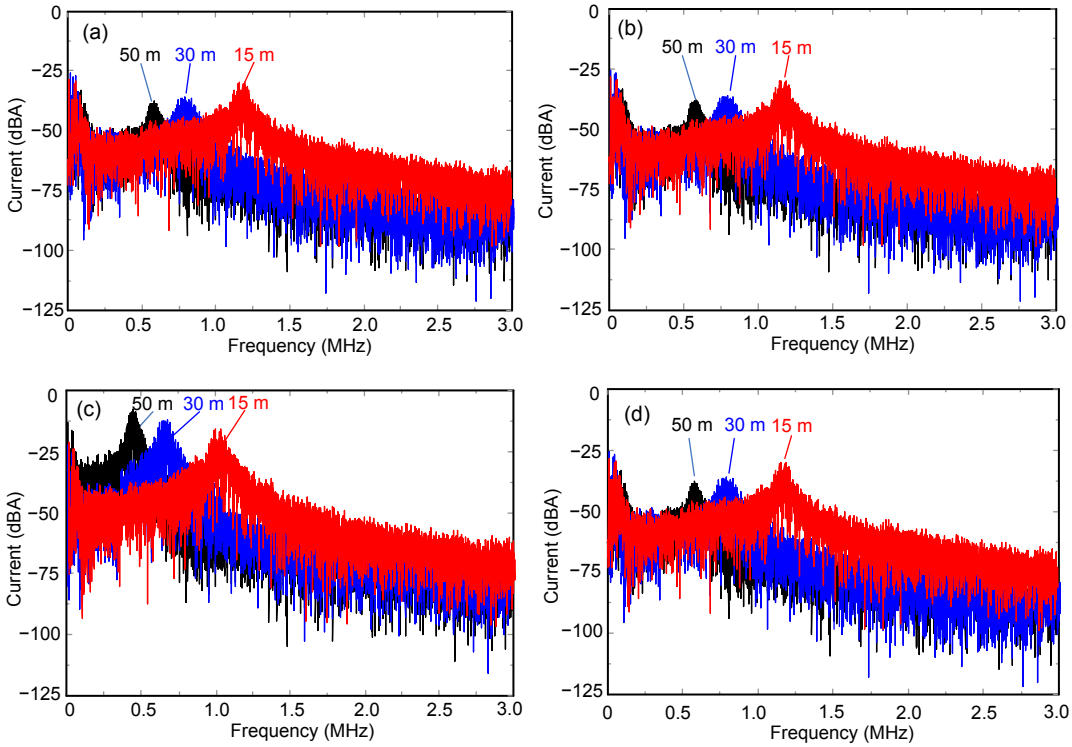

Fig. 15 Frequency spectra of CM currents: (a) three-wire unshielded cable at inverter terminal; (b) three-wire unshielded cable at motor terminal; (c) four-wire shielded cable at inverter terminal; (d) four-wire shielded cable at motor terminal (References to color refer to the online version of this figure)

As shown in Fig. 16b, in the four-wire cable, because of the grounded conductor N, the stray capacitances are much larger, leading to much larger i_{gc}. As a result, i_{CM1} is larger than i_{CM2} in the four-wire cable system. When the cable length increases, the impedance of the CM circuit is smaller and most of i_{CM1} flows through the stray capacitances, and that is why the CM current increases at the inverter terminal and decreases at the motor terminal.

The frequency-domain results are shown in Fig. 15. The resonant frequencies of ASDs can be obtained by $f=1/\sqrt{L_{eq}C_{eq}}$, where L_{eq} and C_{eq} are the equivalent CM inductance and capacitance of the ASD. With the increase in the cable length, L_{eq} and C_{eq} increase, and the dominant frequencies of the CM currents decrease at both the motor and inverter terminals. In the three-wire unshielded cable system, the frequency spectra of the CM currents at the inverter terminal are consistent with those at the motor terminal. In the four-wire shielded cable system, because of the stray capacitances the CM currents increase at the inverter terminal and decrease at the motor terminal when the cable is longer.

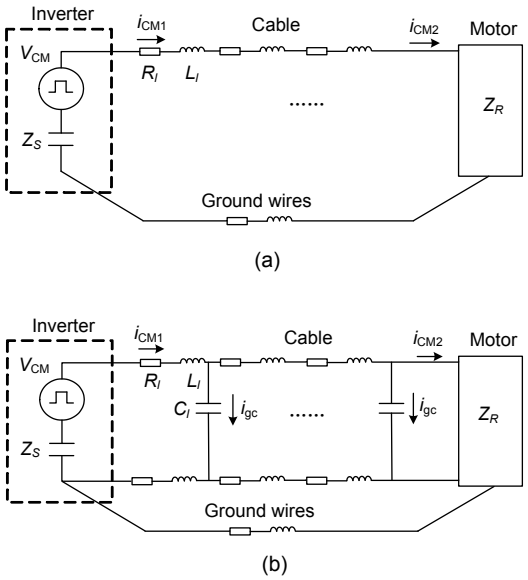

Fig. 16 CM equivalent circuits of ASDs: (a) three-wire cable system; (b) four-wire cable system

V_{CM}: CM voltage source; Z_S: CM impedance of the inverter; Z_R: CM impedance of the motor; R_l, L_l, and C_l: stray resistance, inductance, and capacitance of the cable, respectively; i_{CM1}: CM current at the inverter terminal; i_{CM2}: CM current at the motor terminal; i_{gc}: current flowing through the stray capacitance of the cable

5 Conclusions

In this paper, a high-frequency model of a cable-fed ASD has been proposed. Shielded and unshielded cable models were built. An *R*-*L* ladder circuit was used to model the skin and proximity effects while a *G*-*C* ladder circuit was used to model the dielectric losses. The mutual inductances between the conductors in the unshielded cable were also considered. The cable parameters have been extracted by the finite element method and validated by experiments. A high-frequency motor model and an inverter model were introduced from existing works. Based on these models, the CM currents at the motor and inverter terminals with different motor cables in the ASD were obtained from simulations. The simulated results were validated by measurements.

In the three-wire unshielded cable system, the cable ground capacitance is small. The CM current at the inverter terminal is consistent with that at the motor terminal, which decreases when the cable length is increased. In the four-wire shielded cable system, the cable ground capacitance is larger because of the grounded conductor *N*. The majority of the CM current flows through the cable ground capacitance, so the CM current at the inverter terminal is larger than that at the motor terminal. For a longer cable, the CM current increases at the inverter terminal but decreases at the motor terminal in the four-wire shielded cable system. When the cable length is longer, the resonant frequency decreases with the increase in the cable length in both the three- and four-wire cable systems.

The high-frequency models can be used to predict and evaluate the CM currents in ASDs with different motor cables, which would help in EMI filter design and CM interference suppression of ASDs, and the proposed models can also be used to predict over-voltages at the ASD motor terminals. However, time delays in the ladder-circuit cable models are only approximated, and only straight cables are studied. Modeling for different cable arrangements should be carried out in the future.

References

Amarir S, Al-Haddad K, 2008. A modeling technique to analyze the impact of inverter supply voltage and cable length on industrial motor-drives. *IEEE Trans Power Electron*, 23(2):753-762. https://doi.org/10.1109/TPEL.2007.915773

Cristina S, Feliziani M, 1989. A finite element technique for multiconductor cable parameters calculation. *IEEE Trans Magn*, 25(4):2986-2988. https://doi.org/10.1109/20.34346

de Paula H, de Andrade DA, Ribeiro Chaves ML, et al., 2008. Methodology for cable modeling and simulation for high-frequency phenomena studies in PWM motor drives. *IEEE Trans Power Electron*, 23(2):744-752. https://doi.org/10.1109/TPEL.2007.915759

Erdman JM, Kerkman RJ, Schlegel DW, et al., 1996. Effect of PWM inverters on AC motor bearing currents and shaft voltages. *IEEE Trans Ind Appl*, 32(2):250-259. https://doi.org/10.1109/28.491472

Hafez B, Abdel-Khalik AS, Massoud AM, et al., 2014. Single-sensor-based three-phase permanent-magnet synchronous motor drive system with Luenberger observers for motor line current reconstruction. *IEEE Trans Ind Appl*, 50(4): 2602-2613. https://doi.org/10.1109/TIA.2013.2296625

Hoseini SK, Adabi J, Sheikholeslami A, 2014. Predictive modulation schemes to reduce common-mode voltage in three-phase inverters-fed AC drive systems. *IET Power Electron*, 7(4):840-849. https://doi.org/10.1049/iet-pel.2013.0182

Jiang D, Wang F, Xue J, 2013. PWM impact on CM noise and AC CM choke for variable-speed motor drives. *IEEE Trans Ind Appl*, 49(2):963-972. https://doi.org/10.1109/TIA.2013.2243394

Kerkman RJ, Leggate D, Skibinski GL, 1997. Interaction of drive modulation and cable parameters on AC motor transients. *IEEE Trans Ind Appl*, 33(3):722-731. https://doi.org/10.1109/28.585863

Liu LM, Li H, Hwang SH, et al., 2013. An energy-efficient motor drive with autonomous power regenerative control system based on cascaded multilevel inverters and segmented energy storage. *IEEE Trans Ind Appl*, 49(1): 178-188. https://doi.org/10.1109/TIA.2012.2229687

Lu XY, Zhang SX, Liu C, et al., 2016. Modeling of common-mode current in motor cable of inverter-fed motor drive system. Asia-Pacific Int Symp on Electromagnetic Compatibility, p.511-514. https://doi.org/10.1109/APEMC.2016.7522783

Luszcz J, 2011. Broadband modeling of motor cable impact on common mode currents in VFD. IEEE Int Symp on Industrial Electronics, p.538-543. https://doi.org/10.1109/ISIE.2011.5984215

Luszcz J, 2013. AC motor feeding cable consequences on EMC performance of ASD. IEEE Int Symp on Electromagnetic Compatibility, p.248-252. https://doi.org/10.1109/ISEMC.2013.6670418

Magdun O, Binder A, 2014. High-frequency induction machine modeling for common mode current and bearing voltage calculation. *IEEE Trans Ind Appl*, 50(3):1780-1790. https://doi.org/10.1109/TIA.2013.2284301

Magdun O, Binder A, Purcarea C, et al., 2009. Modeling of asymmetrical cables for an accurate calculation of

common mode ground currents. IEEE Energy Conversion Congress and Exposition, p.1075-1082. https://doi.org/10.1109/ECCE.2009.5316467

Moreau M, Idir N, Le Moigne P, 2009. Modeling of conducted EMI in adjustable speed drives. *IEEE Trans Electromagn Compat*, 51(3):665-672. https://doi.org/10.1109/TEMC.2009.2025269

Moreira AF, Lipo TA, Venkataramanan G, et al., 2002. High-frequency modeling for cable and induction motor overvoltage studies in long cable drives. *IEEE Trans Ind Appl*, 38(5):1297-1306. https://doi.org/10.1109/TIA.2002.802920

Purcarea C, Mutschler P, Magdun O, et al., 2009. Time domain simulation models for inverter-cable-motor systems in electrical drives. 13th European Conf on Power Electronics and Applications, p.1-10.

Saini AS, Nakhla MS, Achar R, 2012. Generalized time-domain adjoint sensitivity analysis of distributed MTL networks. *IEEE Trans Microw Theory Tech*, 60(11): 3359-3368. https://doi.org/10.1109/TMTT.2012.2214053

Tseng SK, Tseng CC, Liu TH, et al., 2015. Wide-range adjustable speed control method for dual-motor drive systems. *IET Electr Power Appl*, 9(2):107-116. https://doi.org/10.1049/iet-epa.2013.0291

Vidmar G, Miljavec D, 2015. A universal high-frequency three-phase electric-motor model suitable for the delta- and star-winding connections. *IEEE Trans Power Electron*, 30(8):4365-4376. https://doi.org/10.1109/TPEL.2014.2352452

Wang LW, Ho CNM, Canales F, et al., 2010. High-frequency modeling of the long-cable-fed induction motor drive system using TLM approach for predicting overvoltage transients. *IEEE Trans Power Electron*, 25(10):2653-2664. https://doi.org/10.1109/TPEL.2010.2047027

Weens Y, Idir N, Bausiere R, et al., 2006. Modeling and simulation of unshielded and shielded energy cables in frequency and time domains. *IEEE Trans Magn*, 42(7): 1876-1882. https://doi.org/10.1109/TMAG.2006.874306